

# A Dual Salt/Dual Solvent Electrolyte Enables Ultrahigh Utilization of Zinc Metal Anode for Aqueous Batteries

Kailin Guan, Wenshu Chen, Yunting Yang, Fei Ye, Ye Hong, Jian Zhang, Qinfen Gu, Yuping Wu, and Linfeng Hu\*

Rechargeable aqueous zinc batteries are promising in next-generation sustainable energy storage. However, the low zinc (Zn) metal anode reversibility and utilization in aqueous electrolytes due to Zn corrosion and poor Zn<sup>2+</sup> deposition kinetics significantly hinder the development of Zn-ion batteries. Here, a dual salt/dual solvent electrolyte composed of Zn(BF<sub>4</sub>)<sub>2</sub>/Zn(Ac)<sub>2</sub> in water/TEGDME (tetraethylene glycol dimethyl ether) solvents to achieve reversible Zn anode at an ultrahigh depth of discharge (DOD) is developed. An “inner co-salt and outer co-solvent” synergistic effect in this unique dual salt/dual solvent system is revealed. Experimental results and theoretical calculations provide evidence that the ether co-solvent inhibits water activity by forming hydrogen bonding with the water and coordination effects with the proton in the outer Zn<sup>2+</sup> solvation structure. Meanwhile, the anion of zinc acetate co-salt enters the inner Zn<sup>2+</sup> solvation structure, thereby accelerating the desolvation kinetics. Strikingly, based on the electrolyte design, the zinc anode shows high reversibility at an ultrahigh utilization of 60% DOD with 99.80% Coulombic efficiency and 9.39 mAh cm<sup>-2</sup> high capacity. The results far exceed the performance reported in electrolyte design work recently. The work provides fundamental insights into inner co-salt and outer co-solvent synergistic regulation in multifunctional electrolytes for reversible aqueous metal-ion batteries.

electrode), high abundance, and intrinsic safety.<sup>[1-3]</sup> These merits have driven the rapid development of aqueous Zn-ion batteries (ZIBs) in recent years as a promising and green technology for high safety and large-scale energy storage.<sup>[4-6]</sup> However, the Zn anode generally suffers from an unsatisfied Coulombic efficiency, and inferior cycling performance with a low Zn anode utilization in aqueous electrolytes.<sup>[6,7]</sup> The main reason lies in the Zn corrosion and hydrogen evolution reaction (HER), which are caused by the reaction of highly reactive water with the Zn metal anode at the aqueous electrolyte-Zn interface.<sup>[4]</sup> Moreover, the slow Zn ion desolvation kinetics at the interface also leads to low anode cycling reversibility at high zinc anode depth of discharge (DOD).<sup>[10,11]</sup>

One critical approach to address the abovementioned Zn anode issues is to decrease the water reactivity and regulate Zn ion deposition kinetics concurrently through interfacial engineering between the Zn metal anode and electrolyte.<sup>[10]</sup>

Recently, tremendous efforts have been devoted to this interfacial engineering and several electrolyte optimization strategies were developed.<sup>[11-14]</sup> First, a high-concentration salt electrolyte normally reduces the amount of active water reacting in the Zn ion solvation structure, leading to reduced HER and corrosion. Unfortunately, such a

## 1. Introduction

Zinc has served as an ideal anode material for aqueous energy storage owing to its high theoretical capacity (820 mAh g<sup>-1</sup>), low electrochemical potential (-0.762 V vs the standard hydrogen

K. Guan, W. Chen, Y. Yang, F. Ye, L. Hu  
School of Materials Science and Engineering  
Southeast University  
Nanjing 211189, P. R. China  
E-mail: [linfenghu@seu.edu.cn](mailto:linfenghu@seu.edu.cn)

Y. Hong  
Industrial Training Center  
Guangdong Polytechnic Normal University  
Guangzhou 510665, China

The ORCID identification number(s) for the author(s) of this article can be found under <https://doi.org/10.1002/adma.202405889>

[Correction added on August 1, 2024, after first online publication: Affiliations has been corrected.]

DOI: 10.1002/adma.202405889

J. Zhang  
State Key Lab of Advanced Technology for Materials Synthesis and Processing  
Wuhan University of Technology  
Wuhan 430070, P. R. China

Q. Gu  
Australian Synchrotron, ANSTO  
800 Blackburn Road, Clayton, VIC 3168, Australia

Y. Wu, L. Hu  
Z Energy Storage Center  
Southeast University  
Nanjing 211189, P. R. China

Y. Wu  
School of Energy and Environment  
Southeast University  
Nanjing 211189, P. R. China

high-concentration salt design generally presents the issues of slow ion transport kinetics.<sup>[12]</sup> Second, water/organic eutectic or pure organic electrolytes formed by using the organic solvent instead of water are developed to eliminate the side reaction for water with the Zn anode.<sup>[13,14]</sup> However, the above electrolyte types lack the inherent fast Zn deposition kinetic advantages of aqueous electrolytes.<sup>[15]</sup> Third, additive-based aqueous electrolytes are designed by adding trace organic/inorganic molecules for adsorbing onto the Zn surface to block water erosion. Nevertheless, additive-based electrolytes usually cannot generate a stable interfacial phase to effectively regulate Zn deposition kinetics.<sup>[16]</sup> Therefore, a multifunctional electrolyte design to simultaneously achieve the suppression of water activity and fast Zn ion desolvation kinetics is highly anticipated but still very challenging.

In general, introducing organic solvents as co-solvents into aqueous electrolytes can effectively decrease the free water proportion and reduce water activity by forming hydrogen bonds with water molecules.<sup>[11,12]</sup> However, the presence of co-solvent in the aqueous electrolyte system usually gives rise to sluggish desolvation and charge transfer kinetics.<sup>[13,14]</sup> Note that the interfacial structure and cationic charge-transfer kinetics can be effectively regulated by various anions from different Zn salts.<sup>[17–19]</sup> Such a consideration inspires us to use more than one salt in the water/organic co-solvent system for realizing highly reversible Zn anode via interfacial engineering from both Zn co-salt and organic co-solvent aspects.

In this work, for the first time, we have proposed a dual salt/dual solvent electrolyte design composed of Zn(BF<sub>4</sub>)<sub>2</sub>/Zn(Ac)<sub>2</sub> in water/TEGDME (/tetraethylene glycol dimethyl ether) with an “inner co-salt and outer co-solvent” synergistic effect. Experimental results and theoretical calculations revealed the TEGDME co-solvent exhibits prominent water reaction suppression due to the formation of hydrogen bonding with the water and the coordination effect with the proton outside the Zn ion solvation shell. The acetate anion of Zn(Ac)<sub>2</sub> co-salt enters the inside Zn ion solvation shell and promotes the desolvation process in the ZnBF<sub>4</sub>-based electrolyte. Moreover, the dual salt/dual solvent design enhances the formation of an efficient inorganic/organic solid electrolyte interface (SEI) on the Zn surface. Consequently, our unique electrolyte achieves impressive Zn anode reversibility of average Coulombic efficiency of 99.80% for 150 cycles at an ultrahigh DOD of 60%. These merits result in outstanding ZIBs performance of high area capacity based on V-based (3.8 mAh cm<sup>-2</sup>) or Mn-based (2.1 mAh cm<sup>-2</sup>) inorganic and PANI (1.2 mAh cm<sup>-2</sup>) organic cathodes, far exceed the performance reported in electrolyte design work recently.

## 2. Results and Discussions

### 2.1. Dual Salt/Dual Solvent Electrolyte Design

A low-cost Zn(BF<sub>4</sub>)<sub>2</sub> salt (denoted as ZnBF, Figure S1, Supporting Information) was first employed in our dual salt/dual solvent electrolyte design. The abundant hydrolysis of the BF<sub>4</sub><sup>-</sup> anions (BF<sub>4</sub><sup>-</sup> + H<sub>2</sub>O ⇌ BF<sub>3</sub>OH<sup>-</sup> + F<sup>-</sup> + H<sup>+</sup>) in the pure aqueous electrolyte (AE) of ZnBF salt (denoted as ZnBF-AE) leads to excessive proton activity, and the protons can transfer via the hydrogen bonding network, resulting in Zn anode corrosion

and HER (Figure 1a).<sup>[20,21]</sup> The experimental observations and Zn//Zn or Zn//Cu half-cell tests at a 20% high depth of discharge of the Zn anode (DOD<sub>Zn</sub>) (Figure S2, Supporting Information) demonstrate that the reversibility and stability of pure aqueous ZnBF electrolyte are inferior to that of some other Zn salts (such as Zn(Ac)<sub>2</sub>, ZnSO<sub>4</sub>, ZnOTF, and ZnCl<sub>2</sub>). However, such a case can be remarkably improved by using a water/organic dual solvent system. The corresponding Zn anode stability results indicate that the Zn metal corrosion resistance and cycling stability of the water/ether (TEGDME co-solvent, denoted as ZnBF-CE) dual solvent electrolyte are better than those of water/sulfone, water/amide, water/nitrile, and water/alcohol systems (Figures S3–S5, Supporting Information). In addition, the Zn//Zn or Zn//Cu cell performance with the water/ether dual solvent electrolyte systems using different Zn salts (ZnSO<sub>4</sub>, ZnOTF, Zn(Ac)<sub>2</sub>, and ZnCl<sub>2</sub>) show that the ZnBF-CE system exhibits the best performance on Zn anode stability and reversibility (Figures S6–S7, Supporting Information). The suppression of zinc anode corrosion by ZnBF-CE electrolyte with the ether co-solvent was further confirmed in the electrochemical Tafel polarization experiment (Figure S8, Supporting Information).

The interaction of the water and ether co-solvent and the functionality of the ether to inhibit Zn corrosion are further considered. In Figure 1b, the hydrogen bonds (H-bonds) are formed via the ether (acting as the hydrogen bond acceptor) and water (acting as the hydrogen bond donor). Thus, the addition of TEGDME ether breaks the H-bonding network of water. The fact is illustrated by Fourier-transform infrared (FTIR) spectra (Figure S9, Supporting Information). The formation of H-bonds reduces the amount of free water, which can attenuate the BF<sub>4</sub><sup>-</sup> hydrolysis reaction. Moreover, the ether breaks the water hydrogen bonding network and can reduce the proton transport by hydrated protons and proton hopping for the Grotthuss mechanism,<sup>[22,23]</sup> thereby avoiding corrosion and HER on the Zn surface. In addition to the role of H-bonds, the ether co-solvent will reversibly coordinate with the proton to form the protonated ether, thus limiting the proton transfer and reducing the proton activity, as shown in Figure 1b. The reversible coordinate binding is because the proton can covalently coordinate with an oxygen atom with the isolated pair electrons on the ether bond (the proton as the electron-pair acceptor of the Lewis acid and the ether as the electron-pair donor of the Lewis base,<sup>[24,25]</sup> Figure S10, Supporting Information). However, the addition of the nonaqueous TEGDME co-solvent will inevitably cause slow charge transfer kinetics due to the reduction of the electrical conductivity for the aqueous electrolyte,<sup>[22,23,26]</sup> resulting in sluggish Zn ion deposition kinetics (Figure 1b).

To address the above kinetics issue, we tried to add a low-cost Zn(Ac)<sub>2</sub> salt (denoted as ZnAc) to enhance the interfacial reaction kinetics of the ZnBF salt electrolyte. First, as a comparison, we tried to add the ZnAc to ZnBF-AE to form ZnBF/Ac-AE with a dual Zn salt/single water solvent system (Figure 1c). The half-cell of ZnBF/Ac-AE measurement shows an improvement in the Zn anode lifetime and Zn plating/stripping efficiency (Figures S11–S13, Supporting Information). This suggests that the ZnBF/Ac-AE system inhibits the Zn corrosion at a certain degree, which is attributed to the lower proton activity resulting from the hydrolysis of adding acetate (Ac<sup>-</sup>) anion (CH<sub>3</sub>COO<sup>-</sup> + H<sub>2</sub>O ⇌ CH<sub>3</sub>COOH + OH<sup>-</sup>) to ZnBF-AE with an increased

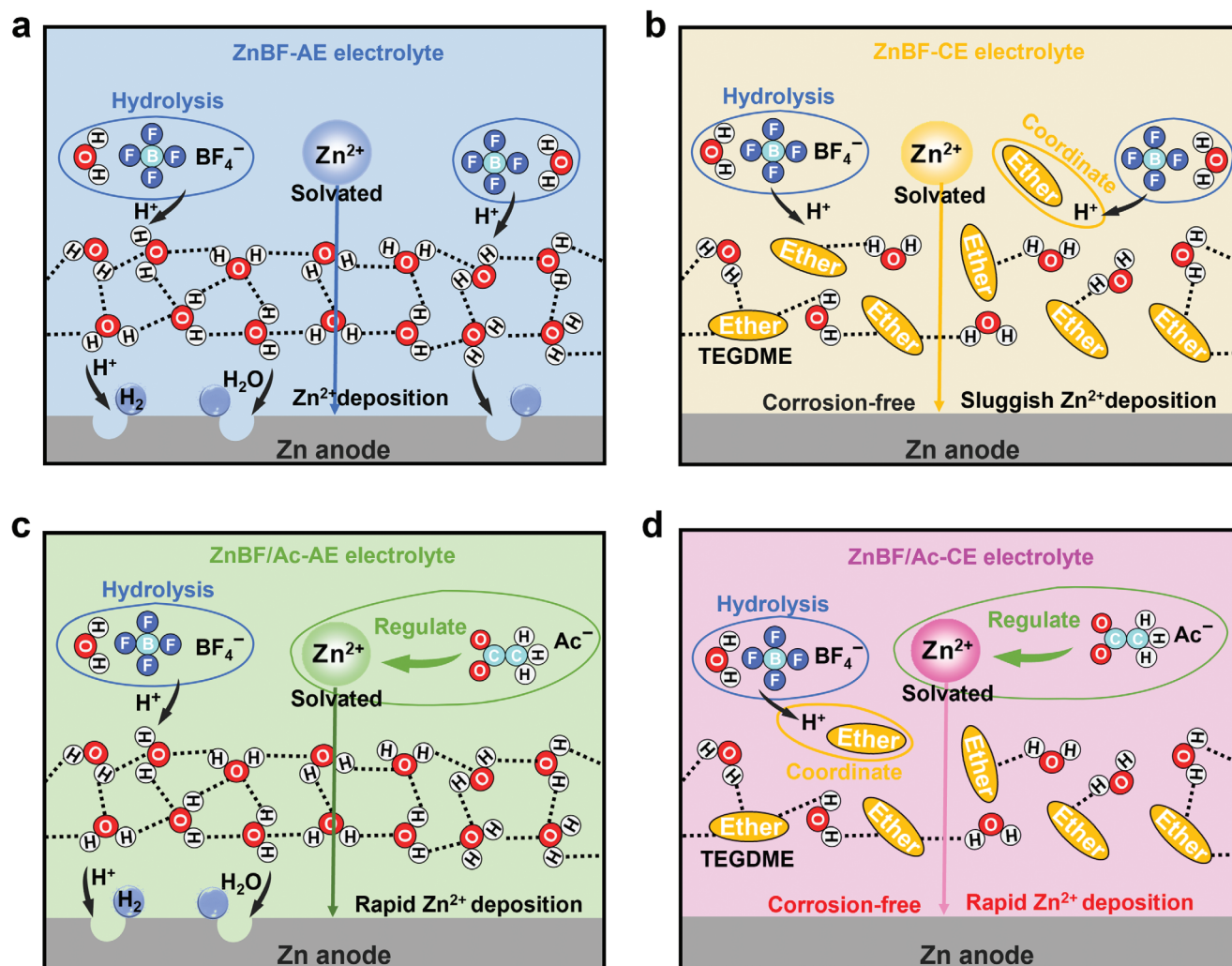


**Figure 1.** Dual salt/dual solvent electrolyte (ZnBF/Ac-CE) design. Schematics of Zn anode interfacial reactions in a) ZnBF-AE, b) ZnBF-CE, c) ZnBF/Ac-AE, and d) ZnBF/Ac-CE electrolytes.

alkalinity. Unfortunately, the ZnBF/Ac-AE system still exhibits unsatisfied cell life and relatively low Coulombic efficiency due to the inability to avoid the corrosion issue of the single water solvent (Figure 1c). However, the experimental results also demonstrate that the ZnBF/Ac-AE system with the dual salt shows rapid Zn ion deposition with lower overpotentials compared to the ZnBF-AE system, indicating that the addition of  $\text{Ac}^-$  regulates the solvated  $\text{Zn}^{2+}$  deposition kinetics (Figure 1c). Furthermore, we added the ZnAc co-salt to that for the ZnBF-CE system (denoted as ZnBF/Ac-CE) aiming to simultaneously avoid Zn corrosion, and accelerate Zn ion deposition, thus enhancing Zn anode reversibility (Figure 1d). The optimal molar ratio between water and TEGDME of 40:1 (Figures S14–S15, Supporting Information) and the optimal molar ratio of ZnBF and ZnAc of 5:1 (Figures S16–S17, Supporting Information) for the ZnBF/Ac-CE electrolyte were obtained from the Zn anode reversibility study. The experimental results in Figures S14–S17 show that the addition of TEGDME and ZnAc in excess will decrease the Zn anode reversibility due to the decrease in ionic conductivity (shown in Figure S18, Supporting Information). The Zn plating/stripping

overpotential is largely reduced at the optimal concentration of ZnAc co-salt in the ZnBF-based electrolyte, indicating the fast Zn/ $\text{Zn}^{2+}$  reaction kinetics in the dual salt electrolyte (Figure S19, Supporting Information).

The effect of the aforementioned four electrolytes on the Zn anode reaction kinetics was subsequently studied by the Zn deposition on Cu electrodes (Figure S20, Supporting Information) and Zn electrodes (Figure S21, Supporting Information) at 0.5, 5, and 10  $\text{mA cm}^{-2}$  rates, respectively. The Zn deposition process includes the  $\text{Zn}^{2+}$  transport by the Zn ions solvation structures, desolvation and charge transfer, and crystalline nucleation at the Zn anode-electrolyte interface. The plating voltage corresponds to the driving force (polarization) required for the Zn deposition and is expressed as the deposition polarization overpotential (denoted as  $\eta$ ), and a larger  $\eta$  reflects slower Zn deposition kinetics.<sup>[27,28]</sup> The Zn deposition profile is shown in Figure S22a (denoting  $\eta_0$  as the initial nucleation polarization overpotential,  $\Delta\eta$  as the nucleation process overpotential when moving from the initial nucleation to the growth stage, and  $\eta_1$  as the polarization overpotential at the growth stage, respectively). The

statistical comparison in Figure S22a, Supporting Information shows that the dual salt electrolytes (ZnBF/Ac-AE and ZnBF/Ac-CE) have smaller  $\eta_0/\Delta\eta/\eta_1$  overpotentials compared to those for the unitary salt electrolytes (ZnBF-AE and ZnBF-CE), which demonstrates the faster Zn nucleation and growth kinetics for the dual salt electrolytes. Moreover, the deposition overpotential of the dual salt electrolytes exhibits no obvious change by changing the current densities and the deposited electrodes, indicating that the fast reaction kinetics property of dual salt electrolytes is intrinsic to the interface, which is further illustrated by the electrochemical cyclic voltammetry test (Figure S22b, Supporting Information) and the rate performance for Zn//Zn cells (Figure S23, Supporting Information). In short, the ZnBF/Ac-CE dual salt/dual solvent electrolyte not only inhibits Zn corrosion but also accelerates the Zn deposition kinetics (Figure 1d, Supporting Information).

The Zn ion solvation structures and electrolyte interactions in the above four electrolytes were investigated to understand further the Zn anode performance enhancement mechanism for our proposed dual salt/dual solvent electrolyte design. The contact angles of the four electrolytes on the Zn surface were first measured to investigate the interfacial interaction (Figure S24, Supporting Information). Results show that the presence of TEGDME co-solvent in the electrolyte system can significantly decrease the interfacial contact angle, while the addition of ZnAc co-salt shows a slight decrease. The decrease in the contact angle should be due to the regulation of water surface tension by TEGDME and  $\text{Ac}^-$ , which reduces the interfacial water amount and breaks the water H-bonds network.<sup>[29]</sup> The TEGDME addition leads to a more significant decrease in the contact angle compared to the  $\text{Ac}^-$ , indicating a stronger effect on the separation of the water H-bonds network. The FTIR spectra further show that the addition of  $\text{Ac}^-$  affects weakly the H-bond structure of water (Figures S25–S27, Supporting Information). Moreover, Raman spectra (Figure S28, Supporting Information) illustrate the four electrolytes (ZnBF-AE, ZnBF/Ac-AE, ZnBF-CE, ZnBF/Ac-CE) have two  $\text{Zn}^{2+}$  solvation structures including the solvent-separated ion pair (SSIP) structure and the contact ion pair (CIP) structure. The SSIP structure is a form in which  $\text{Zn}^{2+}$  would only be coordinated with the solvent ( $\text{Zn}^{2+}\cdot(\text{H}_2\text{O})_x$ ), while in the CIP structure,  $\text{Zn}^{2+}$  would be coordinated with the anions apart from the coordination with the solvent ( $\text{Zn}^{2+}\cdot(\text{BF}_4^-)_y(\text{H}_2\text{O})_z$ ).<sup>[19,30]</sup> The first Zn ion solvation shell is formed by the coordination between cation (as Lewis acid and electron acceptor) and solvent/anion (Lewis base or electron donor).<sup>[10,11,31,32]</sup>

The photographs of the four electrolytes in Figure 2a show both aqueous and co-solvent electrolytes with transparent state. Considering the intense contact of the electrolytes with the Zn electrodes, molecular dynamic (MD) simulations were conducted to clarify the interfacial structure of our rationally designed electrolytes (Figures S29–S30, Supporting Information). The typical first  $\text{Zn}^{2+}$  solvation structures based on dynamics simulations are shown in Figure 2a; and Figure S30, Supporting Information. The radial distribution function (RDF) plots of  $\text{Zn}^{2+}$  are presented in Figure 2b–e. The RDF of the ZnBF-AE (Figure 2b, Supporting Information) shows an average coordination number (CN) of 5.57 for  $\text{Zn}^{2+}\cdot\text{O}(\text{H}_2\text{O})$  and 0.45 for  $\text{Zn}^{2+}\cdot\text{F}(\text{BF}_4^-)$ , respectively, suggesting the presence of CIP structure with  $\text{Zn}^{2+}\cdot\text{BF}_4^-$  coordination and the SSIP structure with  $\text{Zn}^{2+}\cdot\text{H}_2\text{O}$  co-

ordination (Figure S30a, Supporting Information). The RDF of the ZnBF/Ac-AE (Figure 2c) shows a CN of 5.26, 0.56, and 0.18 for  $\text{Zn}^{2+}\cdot\text{O}(\text{H}_2\text{O})$ ,  $\text{Zn}^{2+}\cdot\text{F}(\text{BF}_4^-)$ ,  $\text{Zn}^{2+}\cdot\text{O}(\text{Ac}^-)$ , respectively. The CN value suggests that the coordination of  $\text{Zn}^{2+}\cdot\text{Ac}^-$  in the CIP structure exists in the  $\text{Ac}^-$ -based pure aqueous electrolyte (Figure S30b, Supporting Information). This reveals that the addition of the ZnAc co-salt allows the  $\text{Ac}^-$  to enter into the first  $\text{Zn}^{2+}$  solvation shell. The RDF of the ZnBF-CE (Figure 2d, Supporting Information) shows a CN of 5.52, and 0.53 for  $\text{Zn}^{2+}\cdot\text{O}(\text{H}_2\text{O})$ , and  $\text{Zn}^{2+}\cdot\text{F}(\text{BF}_4^-)$ , respectively. No significant peak appearing at around 2 Å for  $\text{Zn}^{2+}\cdot\text{O}(\text{TEGDME})$  indicates that there is probably no such coordination in the ZnBF-CE (Figure S30c, Supporting Information), showing that the TEGDME co-solvent will not enter into the first  $\text{Zn}^{2+}$  solvation shell. The RDF of the ZnBF/Ac-CE (Figure 2e) shows a CN of 5.58 for  $\text{Zn}^{2+}\cdot\text{O}(\text{H}_2\text{O})$ , 0.20 for  $\text{Zn}^{2+}\cdot\text{F}(\text{BF}_4^-)$ , 0.19 for  $\text{Zn}^{2+}\cdot\text{O}(\text{Ac}^-)$  respectively, suggesting that the ZnBF/Ac-CE forms the CIP coordination form of  $\text{Zn}^{2+}\cdot\text{Ac}^-$ . The RDF of the ZnBF/Ac-CE shows a similar situation for the  $\text{Zn}^{2+}\cdot\text{O}(\text{TEGDME})$  in the ZnBF-CE (Figure 2e). The presence of  $\text{Zn}^{2+}\cdot\text{Ac}^-$  coordination can be derived from the RDF, suggesting that the addition of  $\text{Ac}^-$  competes with  $\text{BF}_4^-$  or  $\text{H}_2\text{O}$  for coordination due to the relatively strong interaction of  $\text{Ac}^-$  with  $\text{Zn}^{2+}$ . The interactions are illustrated by the density functional theory (DFT) calculations on the electrostatic potential (ESP, Figure S31, Supporting Information) and binding energies (Figure 2f; and Figure S30, Supporting Information). Due to the lower electronegativity of  $\text{Ac}^-$  anion ( $\text{Ac}^-$ :  $-7.43$  eV,  $\text{BF}_4^-$ :  $-6.05$  eV,  $\text{H}_2\text{O}$ :  $-1.8$  eV, TEGDME:  $-1.4$  eV, Figure S31, Supporting Information) enables a strong ionic interaction with the cation, the  $\text{Ac}^-$  enters the first Zn ion solvation shell and coordinates with the Zn ion. The almost absence of  $\text{Zn}^{2+}\cdot\text{TEGDME}$  coordination in the dual solvent electrolyte could be attributed to the weak interaction between TEGDME with  $\text{Zn}^{2+}$  compared to the anions of  $\text{BF}_4^-$  and  $\text{Ac}^-$  due to TEGDME is a weak Lewis base with a low donor number (16.6 less than  $\text{H}_2\text{O}$  of 18)<sup>[28,33,34]</sup> and less addition than  $\text{H}_2\text{O}$  solvent (molar ratio of  $\text{H}_2\text{O}/\text{TEGDME}$  in 40/1). Theoretical calculations of binding energies also identify that TEGDME is weakly binding to  $\text{Zn}^{2+}$  compared to anions (Figure S32, Supporting Information). Thus, the  $\text{Ac}^-$  anions with a strong electrostatic effect can join the first  $\text{Zn}^{2+}$  solvation structure for Zn ion transfer regulation, whereas the TEGDME co-solvent molecules with a non-solvating effect for Zn ions located on the outside of the first  $\text{Zn}^{2+}$  solvation structure.

The desolvation steps and desolvation energies for different  $\text{Zn}^{2+}$  solvated structures were ascertained by DFT calculations on free energies (Figure 2h,i; and Figure S33, Supporting Information). The SSIP structure of  $\text{Zn}^{2+}\cdot(\text{H}_2\text{O})_6$  takes the last step of desolvation as  $\text{Zn}^{2+}\cdot\text{H}_2\text{O}$ , which can enable the proximity of  $\text{H}_2\text{O}$  to the Zn surface, leading to corrosion and HER. The low LUMO energy level of  $\text{Zn}^{2+}\cdot\text{H}_2\text{O}$  or  $\text{Zn}^{2+}\cdot(\text{H}_2\text{O})_6$  indicates that the coordinated  $\text{H}_2\text{O}$  is prone to reductive decomposition (Figure 2g; and Figure S34, Supporting Information). The desolvation of  $\text{Zn}^{2+}\cdot(\text{BF}_4^-)(\text{H}_2\text{O})_5$  and  $\text{Zn}^{2+}\cdot(\text{Ac}^-)(\text{H}_2\text{O})_5$  of the CIP structure involves the removal of the  $\text{H}_2\text{O}$  solvent followed by the removal of the anions, and the last desolvation step is in the forms of  $\text{Zn}^{2+}\cdot\text{BF}_4^-$  and  $\text{Zn}^{2+}\cdot\text{Ac}^-$ , respectively (Figure 2h), which cannot be easily prone to HER compared to the SSIP structure. The LUMO (Lowest unoccupied molecular orbital) energy levels reveal that the high energy levels of the CIP structure are not

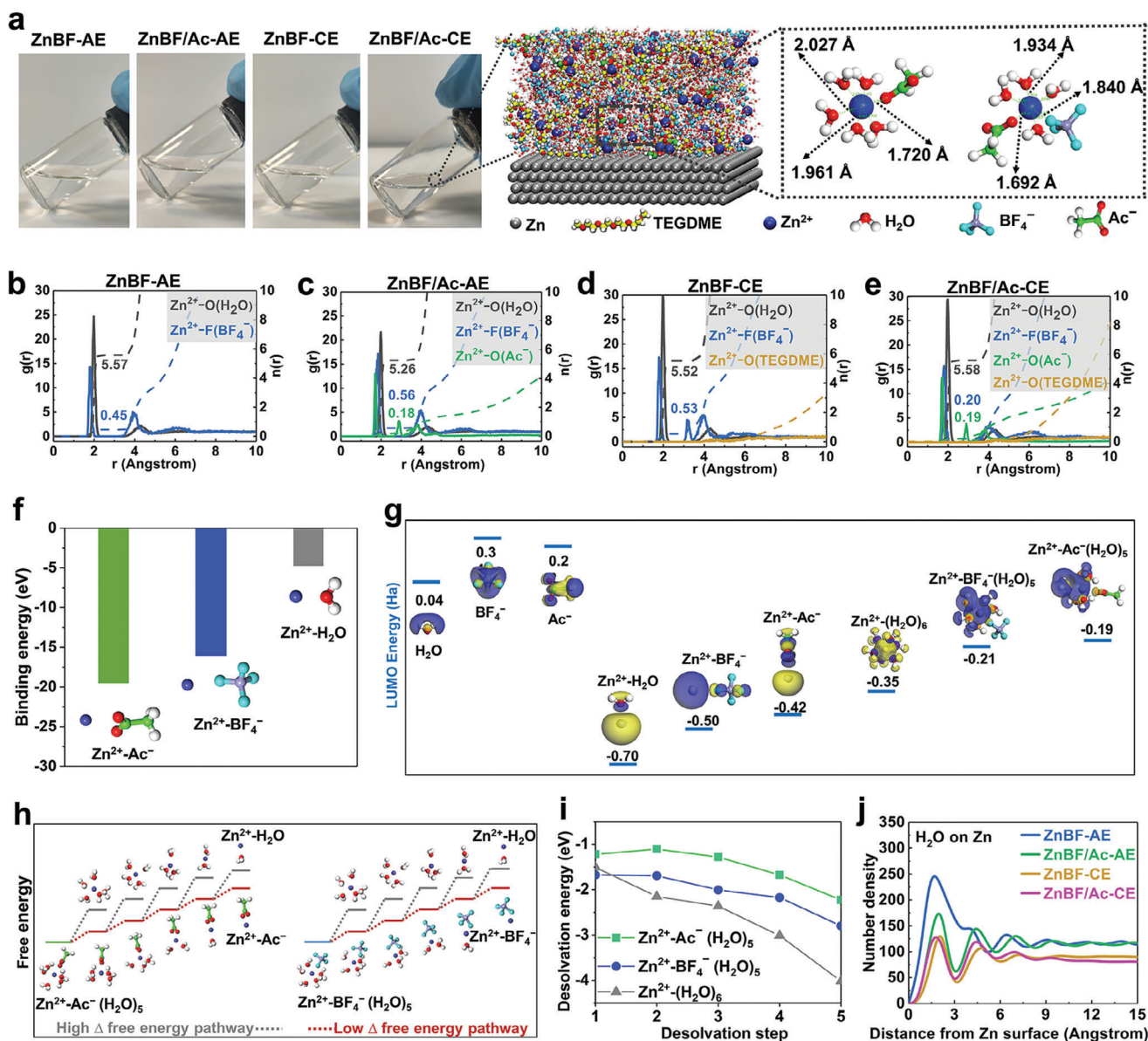


**Figure 2.** Molecular dynamics (MD) simulations and density functional theory (DFT) calculations for the four electrolytes. a) 3D models of interfacial molecular dynamics and typical  $Zn^{2+}$  solvated structures of ZnBF/Ac-CE electrolyte. The C atoms in  $Ac^-$  and TEGDME are differentiated by using a green color for C in  $Ac^-$  and a yellow color for C in TEGDME. The radial distribution function ( $g(r)$ , in solid line) and coordination numbers ( $n(r)$ , in dashed line) of coordinated  $Zn^{2+}$  in b) ZnBF-AE, c) ZnBF/Ac-AE, d) ZnBF-CE, and e) ZnBF/Ac-CE electrolytes. f) Binding energies of  $Zn^{2+}$  with  $H_2O/BF_4^-/Ac^-$ . g) LUMO energy levels for  $H_2O/BF_4^-/Ac^-$  or coordinated  $Zn^{2+}$  solvation structures. h) Desolvation processes and i) desolvation energies for various  $Zn^{2+}$  solvated structures. j) The number density of  $H_2O$  on the Zn surface.

easily reducible compared to the SSIP structure (Figure 2h; and Figure S34, Supporting Information). The addition of  $Ac^-$  into the electrolytes promotes the formation of the CIP structures, leading to the reduced HER reaction. The calculation of desolvation energies (Figure 2i) illustrate that the CIP structures of  $Zn^{2+}-(BF_4^-)(H_2O)_5$  and  $Zn^{2+}-(Ac^-)(H_2O)_5$  are easier to desolvate  $H_2O$  molecules than the SSIP structure of  $Zn^{2+}-(H_2O)_6$ . This shows that the anions entering the  $Zn^{2+}$  solvated structures have fast desolvation kinetics. Moreover,  $Zn^{2+}-(Ac^-)(H_2O)_5$  is more readily to desolvate  $H_2O$  compared to  $Zn^{2+}-(BF_4^-)(H_2O)_5$ , suggesting that the  $Ac^-$  in the solvated  $Zn^{2+}$  structure leads to a faster

rate of dewatering solvation kinetics compared to  $BF_4^-$ . Thus, the  $BF_4^-$ -based electrolytes with increased desolvation rate due to the  $Ac^-$  addition can provide fast Zn ion deposition kinetics and reduces the polarization overpotential of electroplated Zn. Consequently, the reversibility of zinc plating/stripping was effectively improved in the half-cell cycles.

The radial number densities of each component in the aforementioned four electrolytes on the Zn surface were also obtained based on MD simulations (Figure S35, Supporting Information; and Figure 2j). The interaction energies were calculated for each component with the Zn electrode (Figures S36–S37, Supporting

Information). In Figure 2j, the stronger number density peaks of H<sub>2</sub>O for ZnBF-AE and ZnBF/Ac-AE compared to those for ZnBF-CE and ZnBF/Ac-CE indicates a large number of water molecules at the interface of Zn electrodes with ZnBF-AE or ZnBF/Ac-AE electrolytes. The smaller amount of water molecules at the interface of Zn electrodes with the ZnBF-CE or ZnBF/Ac-CE is attributed to the TEGDME adsorption, which can be verified from the number density peak of TEGDME in Figure S35e, Supporting Information. In addition, the Ac<sup>-</sup>-based electrolytes present the Ac<sup>-</sup> adsorption on the Zn surface (Figure S35f, Supporting Information). The above adsorption effects are also inferred from the calculations of the interaction energies of each component with the Zn electrode (Figures S36–S37, Supporting Information). In Figure S37a, Supporting Information, the relatively more negative energies of the H<sub>2</sub>O molecules in ZnBF-AE and ZnBF/Ac-AE compared with those of ZnBF-CE and ZnBF/Ac-CE indicate a stronger interaction of H<sub>2</sub>O with the Zn electrodes. The relatively weaker interaction of H<sub>2</sub>O molecules with the Zn electrode in ZnBF-CE or ZnBF/Ac-CE indicates that the TEGDME adsorption reduces the adsorption number of H<sub>2</sub>O molecules. Compared to ZnBF-CE, the interaction of TEGDME molecules with the Zn electrode is weaker in ZnBF/Ac-CE (Figure S37b, Supporting Information), which is due to the presence of more Ac<sup>-</sup> (Figure S37c, Supporting Information) and BF<sub>4</sub><sup>-</sup> anions (Figure S37d, Supporting Information). The above adsorption effects are also confirmed by the DFT calculations of the adsorption energies (Figure S38, Supporting Information). The most negative adsorption energy of TEGDME with the Zn electrode indicates that TEGDME can preferentially adsorb on the Zn surface relative to H<sub>2</sub>O, thereby reducing the adsorption of H<sub>2</sub>O on the Zn surface. Besides, the TEGDME co-solvent molecules locate outside the first Zn ion solvation shell and forms hydrogen bonds with H<sub>2</sub>O of the first solvated structures to inhibit water reduction activity. Theoretical calculations also show that TEGDME-H<sub>2</sub>O has a stronger binding capacity than H<sub>2</sub>O–H<sub>2</sub>O (Figure S32, Supporting Information). The addition of co-solvent TEGDME reduces water and proton activity, leading to inhibition of zinc corrosion and hydrogen evolution reactions (HER). Therefore, the cells with TEGDME-added co-solvent electrolytes can maintain a long cycling stability. Since the ZnBF/Ac-CE electrolyte with TEGDME and Ac<sup>-</sup> has few H<sub>2</sub>O molecules but many TEGDME/anions at the interface, such an interfacial structure inhibits water activity in the outer of the first Zn<sup>2+</sup> solvation structure, prevents the corrosion and HER side reactions by TEGDME co-solvent. Meanwhile, interfacial Zn<sup>2+</sup> transfer kinetics is accelerated by the ZnAc co-salt, which regulates the inner of the first Zn<sup>2+</sup> solvation structure at the interface. Accordingly, the combination of co-salt and co-solvent forces synergistically regulates the Zn ion solvation structure and the interfacial reaction kinetics.

## 2.2. Zn Anode Stability

To assess the inhibition effect for spontaneous corrosion of the Zn anode by our dual salt/dual solvent electrolyte design, we soaked the Zn foils into the above-mentioned four electrolytes to observe the corrosion behaviors. The photographs of the soaked Zn foils in Figure S39, Supporting Information show the dual salt/dual solvent electrolyte exhibits the best corrosion-

resistant effect. Meanwhile, the soft pack cell storage tests (Figure S40, Supporting Information), self-discharge and capacity storage properties (Figure S41, Supporting Information), and HER experiments (Figure S42, Supporting Information) identify that the dual solvent electrolyte exhibits higher storability and suppressed side reactions, which are attributed to the suppressed water activity by the TEGDME co-solvent. The addition of ZnAc co-salt into the ZnBF-AE or ZnBF-CE electrolyte further reduces the self-corrosion and HER on the Zn surface, which can be ascribed to the hydrolysis of Ac<sup>-</sup> that increases the solution alkalinity, leading to the decrease in proton activeness (Figure S43, Supporting Information).

The Zn transfer kinetic properties at the Zn electrode–electrolyte interface in different electrolytes were further studied by electrochemical impedance spectroscopy (EIS) characterizations. The initial and cycled EIS were measured and circuit fitting was performed for Zn//Zn cells using different electrolytes (Figures S44–S45, Supporting Information). The comparison of fitted resistance for the four different electrolytes is shown in Figure S45c, Supporting Information. In the initial and cycled  $R_s$  comparisons, the dual solvent electrolytes (ZnBF-CE and ZnBF/Ac-CE) may have lowered the ion conductivity compared to the pure aqueous electrolytes (ZnBF-AE and ZnBF/Ac-AE), resulting in slightly increased impedance. Moreover, the  $R_s$  of ZnBF/Ac-AE with Ac<sup>-</sup> is higher than that for ZnBF-AE. However, as shown by the ohm numerical intensities of the  $R_s$ ,  $R_f$ , and  $R_{ct}$ , the intensity of  $R_s$  is excessively smaller in comparison to  $R_f$  or  $R_{ct}$ , indicating that the electrochemical impedance arises mainly from the interfacial resistance and charge transfer resistance, which can also be validated from the impedance comparison of the symmetric Zn//Zn cell and the SS//SS cell (Figure S46, Supporting Information). The  $R_f$  is mainly generated at the after-cycled interface, resulting from either the corroded state of the Zn surface or the SEI formation. The high  $R_f$  after cycling in the ZnBF-AE system may originate mostly from Zn surface corrosion. The largely decreased  $R_f$  for ZnBF/Ac-AE can be explained by a corrosion-reducing effect. The high  $R_f$  after cycling in ZnBF-CE and ZnBF/Ac-CE systems should be attributed to the generation of more SEI with less corrosive conditions. The decrease of  $R_f$  for ZnBF/Ac-CE within Ac<sup>-</sup> may indicate the formation of SEI is favorable for Zn ion transfer. Moreover, the  $R_{ct}$  in the ZnBF/Ac-AE or ZnBF/Ac-CE electrolyte is significantly reduced as compared with those for ZnBF-AE or ZnBF-CE, implying that the presence of Ac<sup>-</sup> at the interface can lead to faster Zn<sup>2+</sup> desolvation and charge transfer characters, thus improving the Zn deposition reaction kinetics. In addition, the larger transfer number of the ZnBF/Ac-CE is due to the faster Zn ion transfer kinetics of the dual salt electrolyte compared to ZnBF-CE electrolyte (Figure S47, Supporting Information).

The Zn anode cycling performance at high capacities and depths of discharge is critical for assessing Zn metal anode utilization for practical application.<sup>[6,8]</sup> The long-term cycling stability is compared for the four studied electrolytes using the half-cells including symmetric Zn//Zn and asymmetric Zn//Cu cells at different DOD<sub>Zn</sub> (Figure 3; and Figures S48–S49, Supporting Information). The Zn//Zn symmetric cell using ZnBF-AE electrolyte delivers a cycle life of only 5 cycles at a 20% DOD<sub>Zn</sub>, while the ZnBF/Ac -AE electrolyte displays an improved lifespan of 28 cycles due to the reduced Zn anode corrosion (Figure 3a).

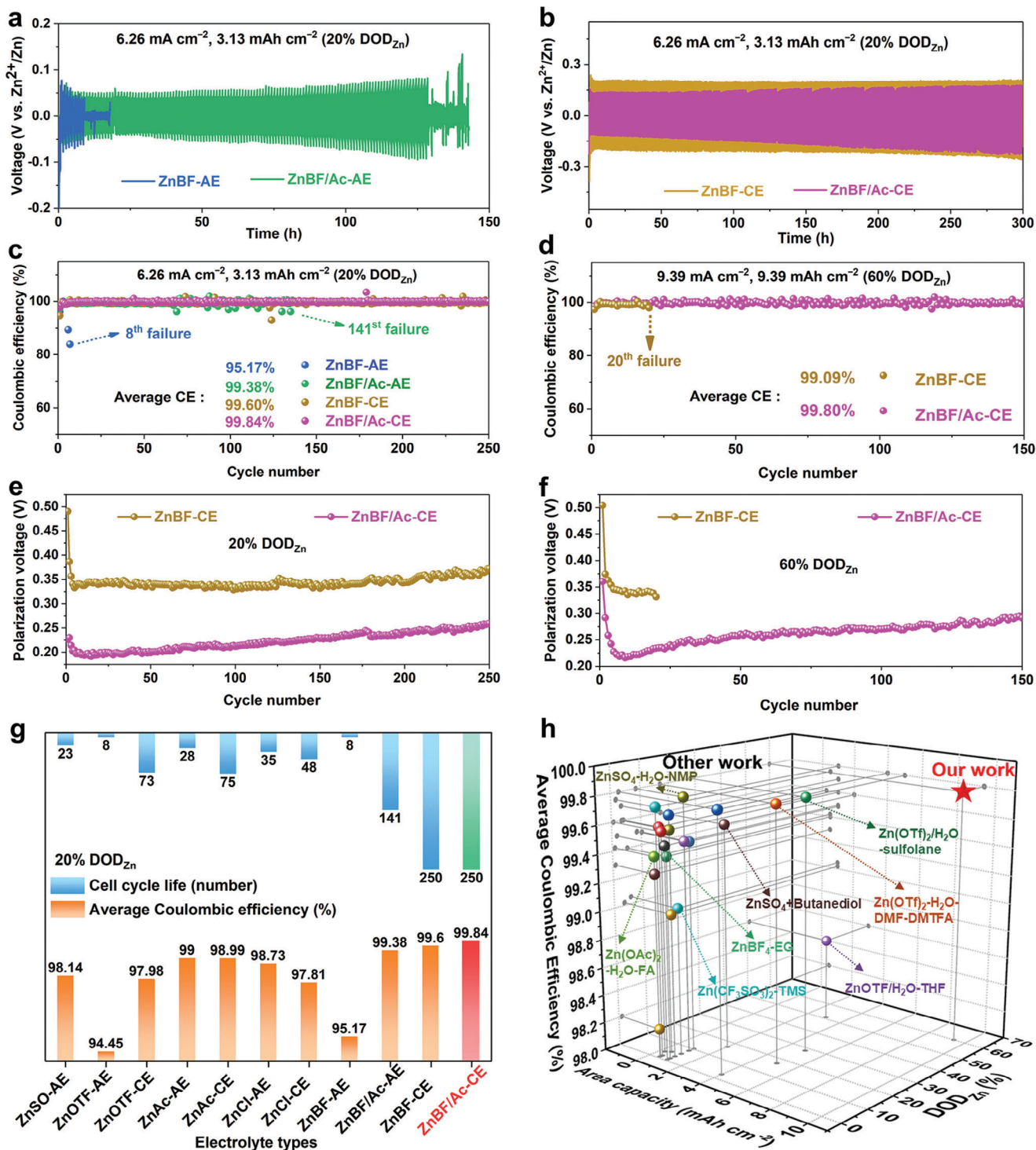


**Figure 3.** The Zn plating/stripping curves of Zn//Zn symmetric cells using a) ZnBF-AE, ZnBF/Ac-AE, and b) ZnBF-CE, ZnBF/Ac-CE electrolytes at a 20% DOD<sub>Zn</sub>. The comparison of Coulombic efficiency of Zn//Cu cells within four electrolytes at c) 20% DOD<sub>Zn</sub> and d) 60% DOD<sub>Zn</sub>. The comparison of polarization voltages in studied electrolytes at e) 20% and f) 60% DOD<sub>Zn</sub>. g) A comparison of Zn plating/stripping Coulombic efficiency for different Zn salt electrolytes. h) A comparison of the Zn anode performance between the dual salt/dual solvent electrolyte in this work and some other recently reported electrolytes.<sup>[22,23,26,37–53]</sup>

Especially, the Zn//Zn symmetric cells containing the ZnBF-CE and ZnBF/Ac-CE electrolytes at a 20% DOD<sub>Zn</sub> shows a much longer cycle life of >300 cycles (Figure 3b).

The average Coulombic efficiencies (ACE) are compared based on the Zn//Cu cells using the four electrolytes at a 20% DOD<sub>Zn</sub> (Figure 3c). The ACE is 95.17% for ZnBF-AE, 99.38% for ZnBF/Ac-AE, 99.60% for ZnBF-CE, and 99.84% for ZnBF/Ac-CE, respectively. The cells within ZnBF-CE or ZnBF/Ac-CE electrolyte have higher Zn plating/stripping efficiency compared with that for ZnBF-AE or ZnBF/Ac-AE electrolyte. The cells with a dual salt electrolyte (ZnBF/Ac-CE) have the highest efficiency at 20% DOD<sub>Zn</sub>. The ACE for ZnBF/Ac-CE remains at 99.80% ACE for 150 cycles (300 h), while the ZnBF-CE has only 99.09% ACE and fails after only 20 cycles (40 h) in a higher DOD<sub>Zn</sub> of 60% (Figure 3d; and Figure S48, Supporting Information). The cells of ZnBF/Ac-CE for 60 DOD<sub>Zn</sub> maintained a high ACE and 50 cycle stability at a 1 mA cm<sup>-2</sup> low current density (Figure S49, Supporting Information). Moreover, the cells with ZnBF/Ac-CE have a high CE in the first cycle (Figure S50, Supporting Information). The Zn plating/stripping polarization voltages (The polarization voltages are equal to the sum of Zn plating voltage and Zn stripping voltage) at 20% or 60% DOD<sub>Zn</sub> for the cells with the ZnBF-CE and ZnBF/Ac-CE electrolytes (Figure 3e,f), demonstrate that the dual salt (ZnBF/Ac) electrolyte substantially reduces the polarization voltage compared to that for the one-salt (ZnBF) electrolyte, indicating the faster Zn deposition/dissolution kinetics for the dual salt electrolyte. In general, the initial Zn stripping/plating requires a high overpotential due to the high electrolyte /interfacial resistance.<sup>[35]</sup> Subsequent Zn stripping/plating cycles are easier than the initial one, corresponding to the decrease of polarization voltages. After a few cycles, the generation of the solid electrolyte interfacial (SEI) phases at the Zn anode surface leads to a slight increase in the polarization voltage.<sup>[36]</sup> These characteristics allow the ZnBF/Ac-CE cells maintain a high reversibility at the higher depths of discharge. The comparison of the cycle performance and ACE for the four electrolytes using other Zn salts (ZnSO, ZnOTF, ZnAc, and ZnCl) demonstrates the universality in achieving high reversibility of the Zn anode employing the dual salt/dual solvent electrolyte of ZnBF/Ac-CE (Figure 3e). In Figure 3f; and Table S1 (Supporting Information), compared with the electrolyte designs from other representative work,<sup>[22,23,26,37–53]</sup> our design of dual salt/dual solvent electrolyte has a prominent advantage for Zn anode performance in simultaneously achieving high capacity, high discharge depth, and high cycle efficiency.

### 2.3. Zn Anode Characterizations

Zn anode characterizations in the four electrolytes were further performed to reveal the cycling stability process and mechanism. The digital photographs in Figure 4a show that after cycling, the Zn surfaces in the ZnBF-AE and ZnBF/Ac-AE electrolytes are severely corroded and feature a large amount of unevenly distributed black dead Zn. In contrast, the Zn surfaces show less corrosion and are flat after cycling in the ZnBF-CE and ZnBF/Ac-CE electrolytes. However, the Zn foil surface after cycling in ZnBF-CE exhibits a large amount of depleted Zn compared to that of the ZnBF/Ac-CE electrolyte, which is attributed to the higher plat-

ing/stripping polarization and slower transfer kinetics for the ZnBF-CE electrolyte. The X-ray diffraction patterns (XRD) of the Zn foils after cycling in the four electrolytes are shown in Figure S51, Supporting Information. Compared with the other three electrolytes, the Zn surface after cycling in ZnBF/Ac-CE electrolyte shows the highest ratio of (002)<sub>Zn</sub>/(101)<sub>Zn</sub>, demonstrating the preferential growth of (002)<sub>Zn</sub> in the ZnBF/Ac-CE electrolyte, thus leading to the flattest morphology, which favors the high Zn anode reversibility.<sup>[54]</sup>

The Zn deposition morphologies in the four studied electrolytes were recorded by in situ optical microscopy (Figure 4b–e). The uneven Zn deposition and corrosion, as well as bubbles generation (H<sub>2</sub> from HER), are observed in the ZnBF-AE electrolyte (Figure 4b). Uneven deposition raised dendrites and corrosion are also observed in the ZnBF/Ac-AE electrolyte (Figure 4c). In contrast, the uniform Zn deposition and refined Zn grains are observed in the ZnBF-CE (Figure 4d) and ZnBF/Ac-CE electrolytes (Figure 4e) electrolytes, which are attributed to the higher deposition overpotential of the dual solvent electrolytes compared to the pure aqueous electrolytes. The higher deposition overpotential leads to a smaller critical nucleation radius, which will refine the grains and induce homogeneous ionic and electronic fields, thereby forming homogeneous deposition morphology.<sup>[27]</sup> In addition, the Zn surface is dense in ZnBF/Ac-CE compared to that in ZnBF-CE, which is related to SEI and will be discussed later. The above Zn deposition morphology changes in the four electrolytes are also illustrated by the cycling performance and phenomenal observations from the in situ transparent cells (Figures S52–S53, Supporting Information).

The Zn surface morphologies after cycling in the four studied electrolytes were observed (Figure 4f–i). The scanning electron microscope (SEM) results are strongly related to previous optical observations (Figure 4a–e). The corroded holes and dendrites, and accumulated dead Zn are observed on the Zn surface after cycling in the ZnBF-AE electrolyte (Figure 4f). Also, raised corroded dendrites grew on the Zn surface can be found after cycling in the ZnBF/Ac-AE electrolyte (Figure 4g). However, the Zn surfaces are devoid of dendrites and corroded morphology after cycling in the ZnBF-CE (Figure 3h) and ZnBF/Ac-CE (Figure 4i) electrolytes. In addition, the Zn surface after cycling in the ZnBF-CE electrolyte exhibits porous morphologies, which are relative to the dense Zn surface after cycling in the ZnBF/Ac-CE electrolyte. The above observations on Zn surfaces after cycling in different electrolytes are also confirmed by the 3D optical profiles (Figure S54, Supporting Information).

The differences in cycled Zn surfaces are correlated with the formation of SEI phases from electrolyte decomposition. X-ray photoelectron spectroscopy (XPS) data with various etching depths were collected (Figure S55, Supporting Information). Time-of-flight secondary ion mass spectrometry (TOF-SIMS) depth profiling was performed to further illustrate the SEI components (Figure 4j–m; and Figures S56–S58, Supporting Information). The normalized density curves of several ionic pattern fragments (ZnF<sup>-</sup>, ZnCO<sub>3</sub><sup>-</sup>, and CH<sub>3</sub>O<sup>-</sup>) for depth profiling of the Zn surface after cycling in different electrolytes as well as the 3D distributions are shown in Figure 4j,k (ZnBF-CE) and Figure 4l,m (ZnBF/Ac-CE), respectively, and the corresponding 2D distributions are presented in Figure S56, Supporting Information. Several ionic pattern fragments (ZnF<sub>2</sub><sup>-</sup>, CO<sub>3</sub><sup>-</sup>, and

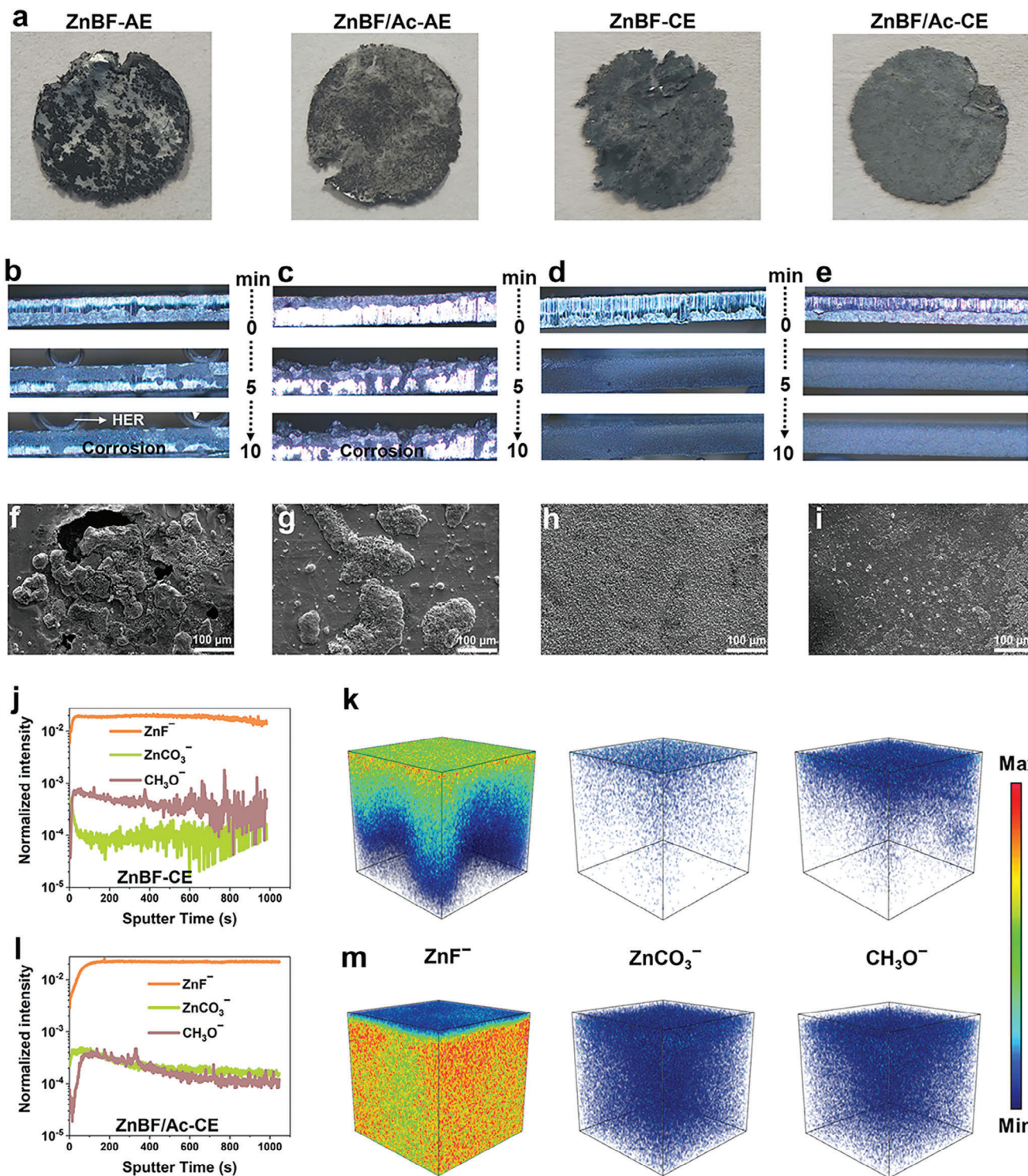


**Figure 4.** Zn anode characterizations in four electrolytes. a) Digital photographs of the Zn anodes after cycling in the four studied electrolytes. Zn deposition process observed by in situ optical microscopy in b) ZnBF-AE, c) ZnBF/Ac-AE, d) ZnBF-CE, and e) ZnBF/Ac-CE electrolytes. SEM images of the Zn surface after cycling in f) ZnBF-AE, g) ZnBF/Ac-AE, h) ZnBF-CE, and i) ZnBF/Ac-CE electrolytes. TOF-SIMS for the depth profiling of several secondary ion fragments and 3D reconstruction of the sputtered volume of the Zn anode surface after cycling in j,k) ZnBF-CE and l,m) ZnBF/Ac-CE electrolytes.

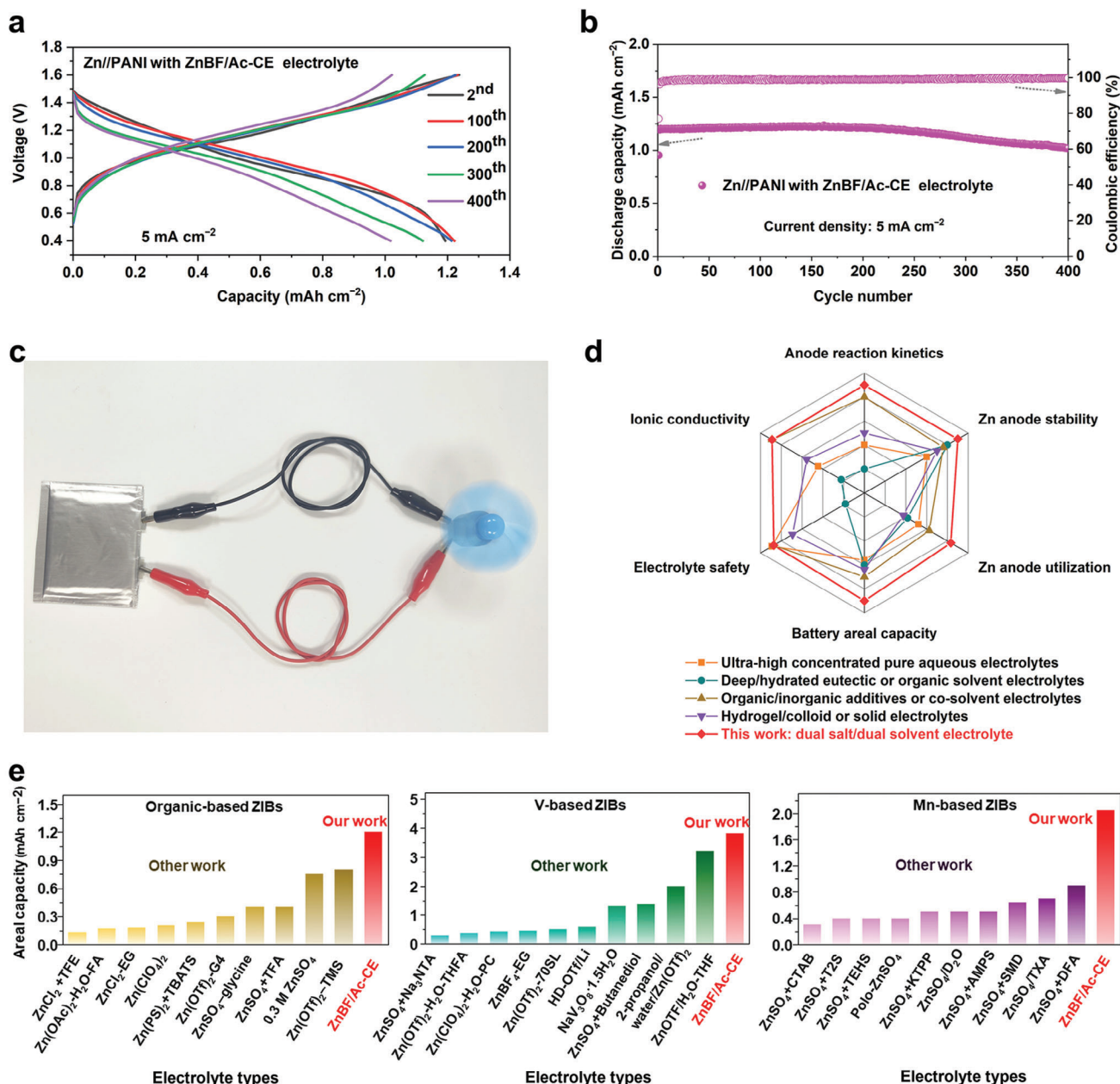


**Figure 5.** ZIBs performance. a) The galvanostatic charging/discharging profiles and b) the cycling stability performance of Zn//PANI batteries with the ZnBF/Ac-CE electrolyte at 5 mA cm<sup>-2</sup>. c) Photograph of an electric fan powered by the pouch ZIBs. d) A comparison on the application properties of the different electrolyte types. e) A comparison on the areal capacity for the ZIBs between the dual salt/dual solvent electrolyte in this work and some other recently reported electrolytes.<sup>[26,38,40,45–47,49–53,61–79]</sup>

CHO<sup>-</sup>) are also shown in Figures S57–S58, Supporting Information. In comparison to ZnBF-CE, the Zn surface and deeper layers after cycling in ZnBF/Ac-CE are distributed with more uniform F-element-containing ZnF<sub>2</sub> inorganics. Moreover, the distribution of uniform C/O-containing inorganics or organics makes the SEI for the Zn surface after cycling in ZnBF/Ac-CE more homogeneous and denser. The results are well in agreement with the SEM and the XPS characterizations. Furthermore, the HRTEM observation also confirms the SEI components with crystallized ZnF<sub>2</sub>, ZnCO<sub>3</sub> and some amorphous or-

ganic phase (Figure S59, Supporting Information). The distribution of Ac<sup>-</sup> at the interface and the involvement of Zn<sup>2+</sup> solvation in the ZnBF/Ac-CE electrolyte can promote the formation of C/O-element-containing substances (e.g., ZnCO<sub>3</sub> or CO<sub>3</sub>-based species). The calculation of the LUMO energy levels in Figure S34 (Supporting Information) illustrates that the Ac<sup>-</sup> involvement of Zn<sup>2+</sup> coordination will readily decompose to SEI-containing CO<sub>3</sub>-based species. Apart from the inorganic SEI component of ZnF<sub>2</sub>, the ZnCO<sub>3</sub> also makes a robust SEI that can resist water erosion and dendrite.<sup>[37,55]</sup> Based on previous SEI studies,<sup>[56]</sup> the uniform

anionic CO<sub>3</sub>-based inorganics contained in the SEI can accelerate the desolvation and charge transfer of cations and lower the transfer energy barriers, thereby speeding up the charge transfer reaction kinetics. It suggests that the Zn surface SEI after cycling in the dual salts/dual solvent electrolyte can utilize the ZnCO<sub>3</sub> derived from acetate decomposition components as well as the ZnF<sub>2</sub> derived from tetrafluoroborate decomposition components to accelerate the desolvation of the solvated Zn ions. In addition, the uniform organic SEI components originating from the decomposition of ether co-solvent in the dual salts/dual solvent electrolyte ensure the flexibility and mechanical stability of the entire SEI.<sup>[57,58]</sup> Overall, the uniform and densely distributed organic–inorganic mixed SEI components are critical for inhibiting Zn corrosion and regulating Zn deposition kinetics over long cycles for the ZnBF/Ac-CE electrolyte.<sup>[59,60]</sup>

#### 2.4. Zn-Ion Battery Performance

The Zn anode stability in the designed electrolytes was further evaluated by assembling ZIBs with ultrathin Zn anode ( $\approx 10\ \mu\text{m}$ ,  $\approx 13\ \text{mg cm}^{-2}$ ) and high-loading cathodes ( $7\text{--}12\ \text{mg cm}^{-2}$ ). The Zn//PANI battery with the ZnBF/Ac-CE electrolyte is superior to the ZnBF-AE, ZnBF/Ac-AE, and ZnBF-CE electrolytes or the pure aqueous electrolytes with other salts for the cycling stability of the batteries (Figures S60–S64, Supporting Information). Moreover, the Zn//PANI battery within the ZnBF/Ac-CE electrolyte performs a higher rate performance (Figure S61, Supporting Information). The Zn//PANI battery with dual salt/dual solvent electrolyte (ZnBF/Ac-CE) shows a  $1.2\ \text{mAh cm}^{-2}$  high area capacity and 85% capacity retention after 400 cycles at  $5\ \text{mA cm}^{-2}$  (Figure 5a,b). The performance of the designed dual salt/dual solvent electrolyte was further verified by testing the Zn//VO<sub>2</sub> (Figures S65–S67, Supporting Information) and Zn//MnO<sub>2</sub> batteries (Figures S68–S69, Supporting Information). The cycling performance and charge/discharge curves for these assembled batteries with different electrolytes are shown in Figures S66–S69, Supporting Information. Compared to the ZnBF-AE, ZnBF/Ac-AE, and ZnBF-CE electrolytes, the Zn//VO<sub>2</sub> and Zn//MnO<sub>2</sub> batteries within the ZnBF/Ac-CE electrolyte maintain the highest capacity and optimal cycling stability. From the above comparisons on the cycle stability performance of Zn//PANI, Zn//VO<sub>2</sub>, and Zn//MnO<sub>2</sub> batteries, it can be concluded that the dual salt/dual solvent electrolyte (ZnBF/Ac-CE) has fast interfacial charge transfer kinetics, leading to the high capacity and cycle stability. As a practical application, Figure 5c shows a pouch Zn//PANI battery with our designed dual salt/dual solvent electrolyte to successfully power an electric fan. Our dual salt/dual solvent electrolytes show significant advances in anode reaction kinetics, zinc anode stability and utilization, and battery capacity upon a qualitative evaluation with other electrolyte types (Figure 5d).<sup>[9,11–14,16]</sup> In addition, comparing the dual salt/dual solvent electrolyte with other designed electrolytes<sup>[26,38,40,45–47,49–53,61–79]</sup> (Figure 5e; and Table S2, Supporting Information), the dual salt/dual solvent electrolyte design attains much higher area capacity in ZIBs based on PANI organic ( $1.2\ \text{mAh cm}^{-2}$ ) or inorganic V-based ( $3.8\ \text{mAh cm}^{-2}$ ), Mn-based ( $2.1\ \text{mAh cm}^{-2}$ ) cathodes at  $0.1$  or  $0.5\ \text{A g}^{-1}$ , demonstrating the superiority of the designed ZnBF/Ac-CE electrolyte.

### 3. Conclusions

In this work, we developed a dual salt/dual solvent electrolyte of Zn(BF<sub>4</sub>)<sub>2</sub>/Zn(Ac)<sub>2</sub> in water/TEGDME with an “inner co-salt and outer co-solvent” synergistic effect to achieve a highly reversible Zn anode at high Zn utilization. Our designed dual salt/dual solvent electrolyte effectively inhibits the Zn corrosion through the TEGDME ether co-solvent by reducing water activity at the outer Zn ion solvation structure. The addition of zinc acetate co-salt promotes the Zn ion desolvation reaction kinetics and boosts SEI formation by the acetate which enters the inner Zn ion solvation structure. Based on this inner co-salt and outer co-solvent synergistic regulation, the designed dual salt/dual solvent electrolyte enables the Zn//Zn or Zn//Cu half-cells to exhibit long cell life and maintain a high Coulombic efficiency of 99.80% at a high Zn anode depth of discharge of 60%. Moreover, high-performance Zn//PANI, Zn//VO<sub>2</sub>, and Zn//MnO<sub>2</sub> batteries were successfully achieved using our designed dual salt/dual solvent electrolyte. Our work provides a novel electrolyte design for high-performance zinc batteries to simultaneously realize the suppression of water activity and the high interfacial Zn ion desolvation kinetics. It also provides fundamental insights into inner co-salt and outer co-solvent synergistic regulation in multifunctional electrolytes for highly reversible aqueous energy storage.

### Supporting Information

Supporting Information is available from the Wiley Online Library or from the author.

### Acknowledgements

This work was financially supported by the National Natural Science Foundation of China (Grant Nos. 52171203, 52371214, 52101261, and 52302224), the Natural Science Foundation of Jiangsu Province (Grant Nos. BK20211516 and BK20221179), the National Key Research and Development Program of China (Grant No. 2021YFB2400400), the Fundamental Research Funds for the Central Universities (Grant No. 2242023K5001), Guangdong Basic and Applied Basic Research Foundation (Grant No. 2021A1515110148), and Special Projects in Universities' Key Fields of Guangdong Province (Grant No. 2023ZDZX3008).

### Conflict of Interest

The authors declare no conflict of interest.

### Data Availability Statement

The data that support the findings of this study are available from the corresponding author upon reasonable request.

### Keywords

aqueous zinc batteries, dual salt/dual solvent electrolyte, zinc anode, zinc reversibility, zinc utilization

Received: April 25, 2024  
Revised: July 1, 2024  
Published online:

- [1] Y. Liang, Y. Yao, *Nat. Rev. Mater.* **2022**, *8*, 109.
- [2] S. W. D. Gourley, R. Brown, B. D. Adams, D. Higgins, *Joule* **2023**, *7*, 1415.
- [3] L. Ma, M. A. Schroeder, O. Borodin, T. P. Pollard, M. S. Ding, C. Wang, K. Xu, *Nat. Energy* **2020**, *5*, 743.
- [4] C. Yang, J. Xia, C. Cui, T. P. Pollard, J. Vatamanu, A. Faraone, J. A. Dura, M. Tyagi, A. Kattan, E. Thimsen, J. Xu, W. Song, E. Hu, X. Ji, S. Hou, X. Zhang, M. S. Ding, S. Hwang, D. Su, Y. Ren, X.-Q. Yang, H. Wang, O. Borodin, C. Wang, *Nat. Sustainable* **2023**, *6*, 325.
- [5] X. Jia, C. Liu, Z. G. Neale, J. Yang, G. Cao, *Chem. Rev.* **2020**, *120*, 7795.
- [6] G. Zampardi, F. La Mantia, *Nat. Commun.* **2022**, *13*, 687.
- [7] L. E. Blanc, D. Kundu, L. F. Nazar, *Joule* **2020**, *4*, 771.
- [8] C. Li, S. Jin, L. A. Archer, L. F. Nazar, *Joule* **2022**, *6*, 1733.
- [9] J. Hao, X. Li, X. Zeng, D. Li, J. Mao, Z. Guo, *Energy Environ. Sci.* **2020**, *13*, 3917.
- [10] L. Yuan, J. Hao, C.-C. Kao, C. Wu, H.-K. Liu, S.-X. Dou, S.-Z. Qiao, *Energy Environ. Sci.* **2021**, *14*, 5669.
- [11] W. Yang, Y. Yang, H. Yang, H. Zhou, *ACS Energy Lett.* **2022**, *7*, 2515.
- [12] S. Chen, M. Zhang, P. Zou, B. Sun, S. Tao, *Energy Environ. Sci.* **2022**, *15*, 1805.
- [13] T. Zhang, Y. Tang, S. Guo, X. Cao, A. Pan, G. Fang, J. Zhou, S. Liang, *Energy Environ. Sci.* **2020**, *13*, 4625.
- [14] C. Liu, X. Xie, B. Lu, J. Zhou, S. Liang, *ACS Energy Lett.* **2021**, *6*, 1015.
- [15] Y. Lv, Y. Xiao, L. Ma, C. Zhi, S. Chen, *Adv. Mater.* **2022**, *34*, 2106409.
- [16] S. Guo, L. Qin, T. Zhang, M. Zhou, J. Zhou, G. Fang, S. Liang, *Energy Storage Mater.* **2021**, *34*, 545.
- [17] Z. Huang, X. Li, Z. Chen, P. Li, X. Ji, C. Zhi, *Nat. Rev. Chem.* **2023**, *7*, 616.
- [18] H. Cheng, Q. Sun, L. Li, Y. Zou, Y. Wang, T. Cai, F. Zhao, G. Liu, Z. Ma, W. Wahyudi, Q. Li, J. Ming, *ACS Energy Lett.* **2022**, *7*, 490.
- [19] L. Miao, Z. Xiao, D. Shi, M. Wu, D. Liu, Y. Li, X. Liu, Y. Sun, S. Zhong, Z. Qian, R. Wang, *Adv. Funct. Mater.* **2023**, *33*, 2306952.
- [20] L. Ma, S. Chen, N. Li, Z. Liu, Z. Tang, J. A. Zapfen, S. Chen, J. Fan, C. Zhi, *Adv. Mater.* **2020**, *32*, 1908121.
- [21] C. Yan, Z. Chen, H. Huang, X. Deng, *Angew. Chem., Int. Ed.* **2023**, *62*, 202300523.
- [22] Q. Meng, Q. Bai, R. Zhao, P. Cao, G. Zhang, J. Wang, F. Su, X. Zhou, J. Yang, J. Tang, *Adv. Energy Mater.* **2023**, *13*, 2302828.
- [23] Y. Wang, T. Wang, S. Bu, J. Zhu, Y. Wang, R. Zhang, H. Hong, W. Zhang, J. Fan, C. Zhi, *Nat. Commun.* **2023**, *14*, 1828.
- [24] L. S. Levitt, B. W. Levitt, *Z. Naturforsch., B.* **1979**, *34*, 614.
- [25] R. Goldie, D. Luck, C. F. Wells, *Phys. Chem. Chem. Phys.* **2003**, *5*, 896.
- [26] D. Han, C. Cui, K. Zhang, Z. Wang, J. Gao, Y. Guo, Z. Zhang, S. Wu, L. Yin, Z. Weng, F. Kang, Q.-H. Yang, *Nat. Sustainable* **2021**, *5*, 205.
- [27] X. Yu, Z. Li, X. Wu, H. Zhang, Q. Zhao, H. Liang, H. Wang, D. Chao, F. Wang, Y. Qiao, H. Zhou, S.-G. Sun, *Joule* **2023**, *7*, 1145.
- [28] M. Kim, J. Lee, Y. Kim, Y. Park, H. Kim, J. W. Choi, *J. Am. Chem. Soc.* **2023**, *145*, 15776.
- [29] Y. Deng, H. Wang, M. Fan, B. Zhan, L. J. Zuo, C. Chen, L. Yan, *J. Am. Chem. Soc.* **2023**, *145*, 20109.
- [30] G. Ma, L. Miao, Y. Dong, W. Yuan, X. Nie, S. Di, Y. Wang, L. Wang, N. Zhang, *Energy Storage Mater.* **2022**, *47*, 203.
- [31] M. Han, J. Huang, X. Xie, T. C. Li, J. Huang, S. Liang, J. Zhou, H. J. Fan, *Adv. Funct. Mater.* **2022**, *32*, 2110957.
- [32] L. Zhou, F. Wang, F. Yang, X. Liu, Y. Yu, D. Zheng, X. Lu, *Angew. Chem., Int. Ed.* **2022**, *61*, 202208051.
- [33] X. Zheng, L. Huang, X. Ye, J. Zhang, F. Min, W. Luo, Y. Huang, *Chem* **2021**, *7*, 2312.
- [34] Y. N. Zhang, F. L. Jiang, F. Bai, H. Jiang, T. Zhang, *ACS Appl. Mater. Interfaces* **2022**, *14*, 10327.
- [35] Q. Li, A. Chen, D. Wang, Y. Zhao, X. Wang, X. Jin, B. Xiong, C. Zhi, *Nat. Commun.* **2022**, *13*, 3699.
- [36] Y. Sui, X. Ji, *Angew. Chem., Int. Ed.* **2023**, *63*, 202312585.
- [37] D. Dong, T. Wang, Y. Sun, J. Fan, Y.-C. Lu, *Nat. Sustainable* **2023**, *6*, 1474.
- [38] C. Li, R. Kingsbury, A. S. Thind, A. Shyamsunder, T. T. Fister, R. F. Klie, K. A. Persson, L. F. Nazar, *Nat. Commun.* **2023**, *14*, 3067.
- [39] W. Xu, J. Li, X. Liao, L. Zhang, X. Zhang, C. Liu, K. Amine, K. Zhao, J. Lu, *J. Am. Chem. Soc.* **2023**, *145*, 22456.
- [40] Q. Ma, R. Gao, Y. Liu, H. Dou, Y. Zheng, T. Or, L. Yang, Q. Li, Q. Cu, R. Feng, Z. Zhang, Y. Nie, B. Ren, D. Luo, X. Wang, A. Yu, Z. Chen, *Adv. Mater.* **2022**, *34*, 2207344.
- [41] Y. Zhong, X. Xie, Z. Zeng, B. Lu, G. Chen, J. Zhou, *Angew. Chem., Int. Ed.* **2023**, *62*, 202310577.
- [42] J. Wan, R. Wang, Z. Liu, S. Zhang, J. Hao, J. Mao, H. Li, D. Chao, L. Zhang, C. Zhang, *Adv. Mater.* **2023**, *13*, 2310623.
- [43] D. Wang, D. Lv, H. Liu, S. Zhang, C. Wang, C. Wang, J. Yang, Y. Qian, *Angew. Chem., Int. Ed.* **2022**, *61*, 202212839.
- [44] C. Chang, S. Hu, T. Li, F. Zeng, D. Wang, S. Guo, M. Xu, G. Liang, Y. Tang, H. Li, C. Han, H.-M. Cheng, *Energy Environ. Sci.* **2024**, *17*, 680.
- [45] M. Wu, X. Wang, F. Zhang, Q. Xiang, Y. Li, J. Guo, *Energy Environ. Sci.* **2024**, *17*, 619.
- [46] C. You, R. Wu, X. Yuan, L. Liu, J. Ye, L. Fu, P. Han, Y. Wu, *Energy Environ. Sci.* **2023**, *16*, 5096.
- [47] Y. Wang, Z. Wang, W. K. Pang, W. Lie, J. A. Yuwono, G. Liang, S. Liu, A. M. Angelo, J. Deng, Y. Fan, K. Davey, B. Li, Z. Guo, *Nat. Commun.* **2023**, *14*, 2720.
- [48] P. Xiong, Y. Kang, N. Yao, X. Chen, H. Mao, W.-S. Jang, D. M. Halat, Z.-H. Fu, M.-H. Jung, H. Y. Jeong, Y.-M. Kim, J. A. Reimer, Q. Zhang, H. S. Park, *ACS Energy Lett.* **2023**, *8*, 1613.
- [49] Z. Shen, J. Mao, G. Yu, W. Zhang, S. Mao, W. Zhong, H. Cheng, J. Guo, J. Zhang, Y. Lu, *Angew. Chem., Int. Ed.* **2023**, *62*, 202218452.
- [50] G. Liang, Z. Tang, B. Han, J. Zhu, A. Chen, Q. Li, Z. Chen, Z. Huang, X. Li, Q. Yang, C. Zhi, *Adv. Mater.* **2023**, *35*, 2210051.
- [51] X. Zhang, Z. Deng, C. Xu, Y. Deng, Y. Jia, H. Luo, H. Wu, W. Cai, Y. Zhang, *Adv. Energy Mater.* **2023**, *13*, 2302749.
- [52] Z. Jiao, X. Cai, X. Wang, Y. Li, Z. Bie, W. Song, *Adv. Energy Mater.* **2023**, *13*, 2302676.
- [53] Y. Shang, V. Kundi, I. Pal, H. N. Kim, H. Zhong, P. Kumar, D. Kundu, *Adv. Mater.* **2024**, *36*, 2309212.
- [54] Z. Huang, Z. Li, Y. Wang, J. Cong, X. Wu, X. Song, Y. Ma, H. Xiang, Y. Huang, *ACS Energy Lett.* **2022**, *8*, 372.
- [55] L. Cao, D. Li, T. Pollard, T. Deng, B. Zhang, C. Yang, L. Chen, J. Vatamanu, E. Hu, M. J. Hourwitz, L. Ma, M. Ding, Q. Li, S. Hou, K. Gaskell, J. T. Fourkas, X. Q. Yang, K. Xu, O. Borodin, C. Wang, *Nat. Nanotechnol.* **2021**, *16*, 902.
- [56] A. Wang, L. Wang, Y. Wu, Y. He, D. Ren, Y. Song, B. Zhang, H. Xu, X. He, *Adv. Energy Mater.* **2023**, *13*, 2300626.
- [57] Y. Shang, N. Chen, Y. Li, S. Chen, J. Lai, Y. Huang, W. Qu, F. Wu, R. Chen, *Adv. Mater.* **2020**, *32*, 2004017.
- [58] Y. Xia, P. Zhou, X. Kong, J. Tian, W. Zhang, S. Yan, W.-h. Hou, H.-Y. Zhou, H. Dong, X. Chen, P. Wang, Z. Xu, L. Wan, B. Wang, K. Liu, *Nat. Energy* **2023**, *8*, 934.
- [59] H. Jiang, L. Tang, Y. Fu, S. Wang, S. K. Sandstrom, A. M. Scida, G. Li, D. Hoang, J. J. Hong, N.-C. Chiu, K. C. Stylianou, W. F. Stickle, D. Wang, J. Li, P. A. Greaney, C. Fang, X. Ji, *Nat. Sustainable* **2023**, *6*, 806.
- [60] Y. Wang, B. Liang, J. Zhu, G. Li, Q. Li, R. Ye, J. Fan, C. Zhi, *Angew. Chem., Int. Ed.* **2023**, *62*, 202302583.
- [61] L. Qian, H. Zhu, T. Qin, R. Yao, J. Zhao, F. Kang, C. Yang, *Adv. Funct. Mater.* **2023**, *33*, 2301118.
- [62] F. Yang, J. A. Yuwono, J. Hao, J. Long, L. Yuan, Y. Wang, S. Liu, Y. Fan, S. Zhao, K. Davey, Z. Guo, *Adv. Mater.* **2022**, *34*, 2206754.
- [63] L. Miao, R. Wang, W. Xin, L. Zhang, Y. Geng, H. Peng, Z. Yan, D. Jiang, Z. Qian, Z. Zhu, *Energy Storage Mater.* **2022**, *49*, 445.
- [64] S. Chen, D. Ji, Q. Chen, J. Ma, S. Hou, J. Zhang, *Nat. Commun.* **2023**, *14*, 3526.

- [65] M. Qiu, P. Sun, K. Han, Z. Pang, J. Du, J. Li, J. Chen, Z. L. Wang, W. Mai, *Nat. Commun.* **2023**, *14*, 601.
- [66] L. Geng, J. Meng, X. Wang, C. Han, K. Han, Z. Xiao, M. Huang, P. Xu, L. Zhang, L. Zhou, L. Mai, *Angew. Chem., Int. Ed.* **2022**, *61*, 202206717.
- [67] R. Wang, M. Yao, M. Yang, J. Zhu, J. Chen, Z. Niu, *Proc. Natl. Acad. Sci. USA* **2023**, *120*, 2221980120.
- [68] Z. Wang, J. Diao, J. N. Burrow, Z. W. Brotherton, N. A. Lynd, G. Henkelman, C. B. Mullins, *Adv. Funct. Mater.* **2024**, *34*, 2311271.
- [69] Y. Qiu, X. Zheng, R. Zhang, Q. Lin, M. Li, J. Luo, S. Yang, Z. Liu, Q. Wang, Y. Yu, C. Yang, *Adv. Funct. Mater.* **2023**, *34*, 2310825.
- [70] H. Tian, J. L. Yang, Y. Deng, W. Tang, R. Liu, C. Xu, P. Han, H. J. Fan, *Adv. Energy Mater.* **2022**, *13*, 2202603.
- [71] J. Yin, H. Liu, P. Li, X. Feng, M. Wang, C. Huang, M. Li, Y. Su, B. Xiao, Y. Cheng, X. Xu, *Energy Storage Mater.* **2023**, *59*, 102800.
- [72] S. Zheng, Y. Wang, B. Luo, L. Sun, G. Duan, J. Huang, Z. Ye, *Chem. Eng. J.* **2023**, *473*, 145313.
- [73] T. Long, Q. Y. Zhao, G. Y. Yin, P. X. Xie, S. Liu, X. Ma, Q. Wu, B. Y. Lu, Z. Dai, X. X. Zeng, *Adv. Funct. Mater.* **2024**, *34*, 2315539.
- [74] X. Gao, Y. Dai, C. Zhang, Y. Zhang, W. Zong, W. Zhang, R. Chen, J. Zhu, X. Hu, M. Wang, R. Chen, Z. Du, F. Guo, H. Dong, Y. Liu, H. He, S. Zhao, F. Zhao, J. Li, I. P. Parkin, C. J. Carmalt, G. He, *Angew. Chem., Int. Ed.* **2023**, *62*, 202300608.
- [75] Y. Yu, P. Zhang, W. Wang, J. Liu, *Small Methods* **2023**, *7*, 2300546.
- [76] K. Yang, H. Fu, Y. Duan, Z. Ma, D. Wang, B. Li, H. S. Park, D. Ho, *ACS Energy Lett.* **2023**, *9*, 209.
- [77] L. Qian, W. Yao, R. Yao, Y. Sui, H. Zhu, F. Wang, J. Zhao, C. Zhi, C. Yang, *Adv. Funct. Mater.* **2021**, *31*, 2105736.
- [78] R. Yao, L. Qian, Y. Sui, G. Zhao, R. Guo, S. Hu, P. Liu, H. Zhu, F. Wang, C. Zhi, C. Yang, *Adv. Energy Mater.* **2021**, *12*, 2102780.
- [79] Z. Liu, R. Wang, Y. Gao, S. Zhang, J. Wan, J. Mao, L. Zhang, H. Li, J. Hao, G. Li, L. Zhang, C. Zhang, *Adv. Funct. Mater.* **2023**, *33*, 2308463.